Published in final edited form as:
Ann Biomed Eng. 2009 September ; 37(9): 1757–1771. doi:10.1007/s10439-009-9749-3.

In Vivo Dynamic Deformation of the Mitral Valve Annulus

Chad E. Eckert[1], **Brett Zubiate**[1], **Mathieu Vergnat**[2], **Joseph H. Gorman III**[2], **Robert C. Gorman**[2], and **Michael S. Sacks**[1]

[1]Engineered Tissue Mechanics and Mechanobiology Laboratory, Department of Bioengineering, Swanson School of Engineering, The McGowan Institute, School of Medicine, University of Pittsburgh, 100 Technology Drive, Room 234, Pittsburgh, PA 15219, USA

[2]Gorman Cardiovascular Research Laboratory, Harrison Department of Surgical Research, University Pennsylvania School of Medicine, Philadelphia, PA, USA

Abstract

Though mitral valve (MV) repair surgical procedures have increased in the United States [Gammie, J. S., *et al. Ann. Thorac. Surg.* 87(5):1431–1437, 2009; Nowicki, E. R., *et al. Am. Heart J.* 145(6):1058–1062, 2003], studies suggest that altering MV stress states may have an effect on tissue homeostasis, which could impact the long-term outcome [Accola, K. D., *et al. Ann. Thorac. Surg.* 79(4):1276–1283, 2005; Fasol, R., *et al. Ann. Thorac. Surg.* 77(6):1985–1988, 2004; Flameng, W., P. Herijgers, and K. Bogaerts. *Circulation* 107(12):1609–1613, 2003; Gillinov, A. M., *et al. Ann. Thorac. Surg.* 69(3):717–721, 2000]. Improved computational modeling that incorporates structural and geometrical data as well as cellular components has the potential to predict such changes; however, the absence of important boundary condition information limits current efforts. In this study, novel high definition *in vivo* annular kinematic data collected from surgically implanted sonocrystals in sheep was fit to a contiguous 3D spline based on quintic-order hermite shape functions with C^2 continuity. From the interpolated displacements, the annular axial strain and strain rate, bending, and twist along the entire annulus were calculated over the cardiac cycle. Axial strain was shown to be regionally and temporally variant with minimum and maximum values of −10 and 4%, respectively, observed. Similarly, regionally and temporally variant strain rate values, up to 100%/s contraction and 120%/s elongation, were observed. Both annular bend and twist data showed little deviation from unity with limited regional variations, indicating that most of the energy for deformation was associated with annular axial strain. The regionally and temporally variant strain/strain rate behavior of the annulus are related to the varied fibrous-muscle structure and contractile behavior of the annulus and surrounding ventricular structures, although specific details are still unavailable. With the high resolution shape and displacement information described in this work, high fidelity boundary conditions can be prescribed in future MV finite element models, leading to new insights into MV function and strategies for repair.

Keywords

Heart valves; Mitral valve; Mitral valve annulus; Biomechanics; Deformation; Cardiac kinematics

Address correspondence to Michael S. Sacks, Engineered Tissue Mechanics and Mechanobiology Laboratory, Department of Bioengineering, Swanson School of Engineering, The McGowan Institute, School of Medicine, University of Pittsburgh, 100 Technology Drive, Room 234, Pittsburgh, PA 15219, USA. msacks@pitt.edu.
Chad Eckert and Brett Zubiate contributed equally to this work.

Introduction

In the past decade, mitral valve (MV) repair has become an increasingly popular therapy for MV pathologies, growing from 38% to over 60% of reported MV intervention procedures.[14,34] Though MV repair has been shown to maintain better ventricular function with fewer associated complications,[5,16,18,47] recent long-term studies using more rigorous definitions of failure have identified less optimistic results for repair durability.[1,11,13,17] In most cases, failures were a result of disruption at the leaflet, chordal, or annular suture lines, suggesting excessive tissue stress and the resulting strain-induced tissue damage as an etiologic factor.

Another essential component of surgical modification of the MV is ring annuloplasty, first introduced by Carpentier in 1969.[10] While repairs without ring annuloplasty are less durable,[5,11] most currently available annuloplasty devices are essentially flat. Thus, when implanted, the rigid and semi-rigid devices only restore the annular geometry in two dimensions with the height of the annulus totally obliterated, thereby placing increased stress and subsequent strain on the repair changes in leaflet shape imposed by annular flattening. The stress induced by annular flattening is likely exacerbated in repairs requiring leaflet resection which further flattens leaflet shape by diminishing the total leaflet tissue area.

Taken as a whole, studies of MV repair suggest that changes in leaflet geometry and the resultant impact on local tissue stress can affect MV tissue homeostasis and potentially alter the long-term repair outcomes. Thus, improvements in valvular treatments are dependent on the establishment of a complete understanding of the function, mechanical properties, and underlying mechanobiological responses of the MV. We are now entering a level of bioengineering knowledge of valvular function wherein computational approaches for practical applications can be realized.[10,28,29] For the MV, recent finite element analyses have clearly shown how computational modeling can provide insight into the cooperative interactions of various MV apparatus components including annular dilation and ring annuloplasty and how these interactions can affect MV tissue stresses.[28,29]

Underlying the mechanobiological response of local tissue stress is the response by the MV interstitial cells (MVIC). As the constituent leaflet cell population, MVICs are believed to perform a variety of functions including cell–cell communication facilitation, wound healing, tissue remodeling, and contraction.[33] These cells also show dual phenotypic characteristics: both fibroblast and smooth muscle-like cells traits are expressed.[12,32,33,45] Further compounding their complexity is a change from predominantly fibroblastic cell expression in healthy adult valves to “activated” myo-like cells displaying contraction in fetal and diseased valves.[37] It is thought that such a change is responsible for active remodeling of the extracellular matrix (ECM). Additionally, VIC phenotype may relate to tissue remodeling demands.[36]

Undoubtedly, improved MV modeling necessitates understanding of MVIC function as related to tissue stress states and requires incorporation of this knowledge in a multi-scale model. As a result, it will become necessary to connect the organ-scale simulations to evaluate our understanding of mechanotransduction, and it would be beneficial to develop MVIC phenotypic/biosynthetic models linked to organ-level deformations. However, there is currently a paucity of quantitative data in the heart valve literature detailing the relation between regional tissue stress, cellular function, and tissue homeostasis. Moreover, while showing much promise, fully dynamic coupled solid–fluid heart valve models are still in development and will require extensive validation before becoming practical. The next logical step is thus to focus on quasi-static models that incorporate collagen architecture, accurate material models, and highly accurate valvular geometry including that of the

annulus, leaflets, and chordae tendons. Though quasi-static approaches simulate only the events which occur after the MV is fully coapted, they are consistent with the hypothesis that MV tissue failure results from abnormally high stresses (from disease or improper repair) and that the greatest tissue stresses occur at full systolic loading.

A lack of quantitative information on the highly dynamic boundary conditions of the functioning MV apparatus reveals a limitation of the present modeling efforts. In particular, the annulus, a dense connective tissue ring surrounding the MV orifice, is known to deform considerably during the cardiac cycle.[46] Yet, despite extensive studies[2,9,15,19,23,28,29,46] a complete description of MV annular kinematics over a cardiac cycle remains lacking. In the present work, we utilized high fidelity 3D positions of ultrasound transducers implanted in the ovine MV annulus to quantify the complete 3D kinematics of the MV annulus under normal cardiac conditions.

Methods

Transducer Implantation

Animal implantation followed the methods of our previous studies.[38,39] Briefly, in compliance with guidelines for humane care (NIH Publication No. 85-23, revised 1985) eight male Dorsett sheep (35–45 kg) were induced with sodium thiopental (10–15 mg/kg IV), intubated, anesthetized, and ventilated with isofluorane (1.5–2%) and oxygen. The surface ECG and arterial blood pressure were continuously monitored. While on cardiopulmonary bypass (CPB), a sterile left lateral thoracotomy was performed, and twelve two millimeter hemispherical piezoelectric transducers (Sonometrics, London, Ontario) were sutured around the annulus (Fig. 1a). The transducer wires were brought out through the atriotomy incision, the atriotomy was closed, and the animals were weaned from CPB. Transducer wires were then brought out through the thoracotomy incision and attached to access buttons sutured to the skin remote to the incision site. Animals were allowed to emerge from anesthesia and recover.

After a seven-day recovery, the animals were anesthetized, and the sonocrystal transducer wires were connected to a Sonometrics Series 5001 Digital Sonomicrometer (Sonometrics Corp., London, Ontario). A high-fidelity transducer (SPC-350, Miller Instruments Inc., Houston, TX) was inserted though a cut-down into the left ventricle via the left carotid artery, and left ventricular pressure was continuously monitored. A catheter-based direct pressure transducer placed in a peripheral artery was used to obtain aortic blood pressure to evaluate hemodynamic function during anesthesia and to guide critical care decisions. As described previously,[19] sonomicrometry array localization (SAL) was used to determine the three-dimensional coordinates of each transducer every 5 ms throughout the cardiac cycle. With this setup, spatial resolutions of the crystals approached 0.024 mm. Three-dimensional sonomicrometry positional data was taken following neosynephrine infusion titrated to achieve systolic blood pressures of 150 mmHg. Ventilation was suspended during sonomicrometry measurements. Data was taken for fifteen contiguous cardiac cycles for each data set. Since cycle-to-cycle variations were extremely small, the last cycle was routinely chosen as representative.

Annulus Curve Fit

The MV annulus essentially forms a three-dimensional space curve which undergoes complex deformations over the cardiac cycle. As a result, it does not lend itself to simplified geometric approximations. Thus in the present study, we developed a generalized approach to approximate the instantaneous annular shape using quintic order shape functions[42] to provide C^2 continuity (continuous to the second derivative). This approach allows for a fully

generalized analysis of annular deformations lacking kinematic restrictions. The curve fitting process had a number of important steps. First, the 3D sonocrystal positional data was rotated such that the annular plane-of-best-fit was aligned with the *XY*-plane. This was accomplished by computing the eigenvectors of the covariance matrix formed based on the Cartesian coordinates of the crystal data centered on the origin. Next, the rotated sonocrystal data was transformed into cylindrical coordinates to reduce the number of dependant variables from three (x, y, z) to two (r, z) with $\theta = 0$ set to sonocrystal 1 (Fig. 1b).

With the data properly oriented, the closed space curve representing the instantaneous MV geometry was divided into three 1D finite elements of equal size defined by the independent variable θ. The finite element that was used to perform the space curve fit was derived from the 1D quintic hermite element originally developed for use in 3D anatomic surfaces.[42] Each 1D element has two nodes and six associated interpolation functions N_j^i (Appendix A), where the subscript $j = 1, 2$ indicates the node number and the superscript $i = 0, 1, 2$ the order of the derivative with respect to $\xi \in [-1,1]$ a single local isoparametric coordinate. Thus, N_j^i weigh six quantities (three per node for two nodes), defined as the main variable and its first and second derivatives with respect to the local coordinate ξ. A quintic order element was chosen since C^2 continuity is assured by having the first and second derivatives defined and continuous at the nodes, insuring that both strain and curvature are continuous functions. Note that the actual nodal derivatives which are intrinsically expressed with respect to ξ are scaled by a factor $d\theta/d\xi$ so that they are continuous in θ. In the present study, $r(\theta)$ or $z(\theta)$ components of the annular coordinates are fit separately.

For the annulus, the problem is to determine the values of the two sets of six nodal variables (for the r and z coordinates, respectively) that yield the best overall interpolation of the function at any point ξ along the element. However, a common problem with high order fits is oscillations of the curve that result from sparse and/or unevenly spaced data. The sonocrystal data is both sparse and variable in density, and as a result, the fit utilizing the Euclidian norm alone could predict an unrealistically tortuous curve. As in previous studies,[22,42,48] the solution is to introduce a Sobolev penalty function that restricts the minimization of the predicted coordinate error $E(X)$, where X represents the coordinate that is being fit, using

$$E(X)=\sum_{\mathrm{p}-1}^{n}|X\left(\xi_{\mathrm{p}}\right)-X_{\mathrm{p}}|^{2}+\int S\ [X\,(\xi)]\,d\xi. \tag{1}$$

Here, the first term on the right hand side represents the conventional Euclidian norm with summation over n data points (i.e., the standard least squares solution), and X is the r or z coordinate. Note that it is understood that the integral in Eq. (1) is performed over all elements. The second term is the integral of the Sobolev norm S, defined by

$$S=A\left(\frac{\partial X}{\partial \xi}\right)^{2}+B\left(\frac{\partial^{2} X}{\partial \xi^{2}}\right)^{2}, \tag{2}$$

where A and B are specified element level constants. The effect of the Sobolev norm is to restrict the length (through the parameter A) and curvature (through parameter B) in each element at the expense of the error function so that the overall fit can be stabilized. Both Sobolev parameters depend on the coordinate system being used and the data density

available per element and thus vary if the number of crystals per element changes (see the next section for detailed methods of determining the optimal Sobolev parameters). With smoothing included, a generalized least squares regression method (Appendix B) was used to determine the nodal parameters for each element and best fit the experimental data.

Fit Validation

In order to independently develop the necessary smoothing criteria, a 3D space curve "phantom" with geometric characteristics similar to the native annulus was created. The phantom acted as a smooth shape prior to fitting. In this case the phantom had an elliptical projection on the *XY*-plane and a pronounced saddle shape similar to the actual annulus geometry. The following system of equations was found to produce suitable curves,

$$\begin{aligned} 1&=\frac{(x-x_0)^2}{a^2}+\frac{(y-y_0)^2}{b^2}\\ z&=c\cdot\cos(\theta)^2+2\cdot\sin(\theta)+z_0 \end{aligned} \tag{3}$$

The phantom was generated by picking $a = 13.5$ and $b = 12.5$, with $c = 7$ to develop an anatomically realistic saddle shape. Evaluating the phantom functions at the same angular positions as the data generated a phantom data set described by a quadratic function and a function of sinusoids. Once the phantom data was fit, the curvature distribution of the phantom was determined to guide the permitted distribution range of the computed annulus. To insure the curvatures were reasonable within the computed model, two optimization criteria were defined: minimization of the mean square error of the curvature distribution and prevention of peak curvature exceeding the peak curvature of the phantom data fit. The first criterion kept the curvature distribution as smooth as possible, while the second criterion limited any regions of artificially high curvature. Optimal values for the Sobolev parameters were determined from the known curvature of the phantom using the Powell method as previous described.[42] In this algorithm, a function, defined in terms of the sum of squares difference of the computed and phantom curvature, was minimized by iteratively refining the value of the function parameters. In cases were anomalous crystals were removed, new Sobolev parameters were computed based on the altered element data density. This procedure of estimating the Sobolev parameters prepared the fit for analysis.

Annular Twist, Bend, and Height

With the annulus space curve generated from the described generalized computational method, a variety of different annular deformation modalities could be investigated. Two such important modalities included twist and bend. For these, 300 evenly distributed points were created based on the curve fitting results. At each point, the local Frenet frame was calculated from the discrete change in parameterized arc length. Tangent $\bar{T}(s)$, normal $\bar{N}(s)$, and binormal $\bar{B}(s)$ vectors were determined for each point around the annulus using

$$\overline{T}(s)=\frac{\frac{dR(s)}{ds}}{\left|\frac{dR(s)}{ds}\right|},\ \overline{N}(s)=\frac{\frac{dT(s)}{ds}}{\left|\frac{dT(s)}{ds}\right|},\ \overline{B}(s)=\overline{T}(s)\times\overline{N}(s). \tag{4}$$

These values were then used to calculate a value of twist ω (degree/mm)

$$\omega = \frac{\operatorname{a\,cos}\left(\frac{\overline{N}(s)_{i,j}\cdot\overline{N}(s)_{i,j+1}}{\left|\overline{N}(s)_{i,j}\right|\left|\overline{N}(s)_{i,j+1}\right|}\right) - \operatorname{a\,cos}\left(\frac{\overline{N}(s)_{i,j}\cdot\overline{N}(s)_{i,j-1}}{\left|\overline{N}(s)_{i,j}\right|\left|\overline{N}(s)_{i,j-1}\right|}\right)}{s_1 + s_2} \tag{5}$$

where i represents a time point, j represents a position along the annulus, and s_1 and s_2 represent arc length values between j and $j + 1$ and between j and $j - 1$, respectively. The calculated value provides an angle change per arc length change (degree/mm) useful in quantifying how successive annular points twist with relation to one another through time. The local bend γ (degree/mm) was computed using

$$\gamma = \frac{\operatorname{a\,cos}\left(\frac{\overline{B}(s)_{i,j}\cdot\overline{B}(s)_{i,j+1}}{\left|\overline{B}(s)_{i,j}\right|\left|\overline{B}(s)_{i,j+1}\right|}\right) - \operatorname{a\,cos}\left(\frac{\overline{B}(s)_{i,j}\cdot\overline{B}(s)_{i,j-1}}{\left|\overline{B}(s)_{i,j}\right|\left|\overline{B}(s)_{i,j-1}\right|}\right)}{s_1 + s_2} \tag{6}$$

where i, j, s_1, and s_2 represent the same values as Eq. (5). The calculated value, in angle change per arc length change, provides a quantitative method of assessing annular bending throughout the cardiac cycle.

A metric for evaluating height around the annulus was computed by fitting a plane intersecting both crystals 1 and 7 (commissure regions) and parallel to crystals 4 and 10 (mid-anterior and mid-posterior regions) and then calculating the distance from each crystal to the plane. With this metric, annular height at each crystal was based on a common reference of the commissures for each time point in the measure cardiac cycle. Height from each data set was normalized to the largest measured value; time was normalized based on LVP. Mean normalized height and standard error of the mean was calculated. Additionally, annular crystal height was computed using previously described techniques.[19,40] Using this method, a plane of best fit was determined from all crystal coordinates by means of an orthogonal distance regression algorithm. The data was then rotated so that the X-axis of the plane bisected the mid-anterior and mid-posterior annular crystals. Height change was computed as the difference between crystal maximum and minimum Z-axis values.

Computation of Regional Strain and Strain Rates

To compute the annular deformation modality of strain, the computed space curve was reparameterized in terms of arc length using

$$s = \int_0^{\theta} \sqrt{r(\theta)^2 + z(\theta)^2}\, d\theta. \tag{7}$$

With this, the annular strain is defined as a change in length along a local tangent. As such, local strains were computed by normalizing differential segments $\Delta(\theta)$ of arc length by the corresponding differential segment in the reference configuration as defined by minimum left ventricular pressure

$$\zeta(\theta) = \left(\frac{\Delta s(\theta)}{\Delta s_0(\theta)} - 1\right) \tag{8}$$

and expressed in percent. Using forward divided differences, strain rate was computed at each annular arc length differential segment $\Delta(\theta)$ where $\zeta(\theta)$ was computed. Strain and strain rate values for all eight animals were averaged based on crystal number; standard error of the mean was calculated along 10 evenly spaced points from each crystals' average strain/strain rate plots.

Results

Fitting Ability

The quintic order Hermite shape functions were more than adequate for capturing the complex shape of the annulus. The radial and height components of the data were fit with exceptional accuracy. Although the quality of the *Z*-component fit is better than the radial component, neither fit dropped below $r^2 = 0.95$. More noteworthy is the ability of the fit to faithfully reconstruct the MV annulus geometry; in particular, its saddle shaped features are well represented. In two animals, single anomalous crystals introduced significant unreasonable errors and were removed. In a third separate animal, two anomalous crystals were removed due to dislocation following surgical implantation. Post-mortem inspection of the crystals in question confirmed dislocations in all three animals. With slightly more aggressive smoothing parameters determined for the altered element data densities based on the previously described methods,[42] the disruption of fit was largely overcome in all three animals. Values for r^2 in these reduced data sets were within ±0.1 of the full data sets.

The curve representing the annulus defines two different areas: the orifice area (the area defined by the area of the cylindrical component position vectors) and the ejection area (the area of the orthogonal annular projection onto the *XY* plane). Both the orifice and ejection areas change with similar trends, though the curves are offset by a separation that is fairly consistent over time (Fig. 2). Though slight differences in annular height are observed between specific crystals (for example, crystal 2 has a maximum mean normalized height of 0.245 ± 0.052 while crystal 3 has a maximum mean normalized height of 0.489 ± 0.107), each individual crystal shows minimal change in height throughout the cardiac cycle (for example, crystal 3 shows a mean normalized height variation of 0.431 ± 0.115 to 0.489 ± 0.107); in most cases, crystal height at a given annular position only varied by approximately 15% of the peak crystal height during a given cardiac cycle. Values computed from the second described algorithm were similar, showing slight differences in crystal height from different annular positions, but showing relatively small (near 15%) variations at the same annular location over the cardiac cycle.

To elucidate regional behavior of the MV annulus, strain of a representative data set is presented in the form of a contour plot (Fig. 3) with red hues indicating positive strain (dilation) and blue hues indicating negative strain (contraction). Computed strain around the annulus at different timepoints is presented with the associated LVP, and crystal locations are labeled in the first timepoint for reference. Both the complex geometry of the annulus and the varied regional strains are apparent from this plot. Regions near the posterior leaflet show a highly contractile nature while little strain variation is observed at the commissure regions. To better quantify strain values at discrete annular locations, a series of representative plots is presented (Fig. 4) showing strain vs. radial position on the annulus. Each plot can be mapped to an associated point on the LVP plot. With this, the extent of the dynamic annular strain can be observed: strains around the annulus for a given pressure can vary by as much as 14% strain between regions. As in the contour plots (Fig. 3), the largest strains are seen near the posterior crystal locations; the commissure crystals show the least amount of variation throughout the LVP points showing a difference of less than 5% strain. Average strain, presented as mean ± standard error of the mean for individual crystals vs. normalized time is shown in Fig. 5 (the number of measured samples is eight, unless

otherwise noted). In the most dynamic crystals (those along the posterior leaflet), average strains ranged from nearly 4 to −14% with the greatest contraction occurring during peak LVP. Crystals near the commissures (notably crystals 2 and 6) showed average strains ranging from 3 to −4%, a substantially smaller difference as compared to the posterior crystals. Mid-anterior leaflet crystals showed moderate average strain changes with peak average dilation at 4% and peak average contraction at −5%.

Similar to the strain results, the strain rates exhibit the same periodic behavior (Fig. 6). As in the corresponding strain plots, the strain rates start and end at unity for all crystal locations. Cursory inspection of the local strain rates vs. time reveal that the tissue moves extremely fast. With contractile rates approaching −100%/s and dilation rates approaching 120%/s (Fig. 7), these results further demonstrate that the MV complex is highly dynamic and rapidly reaches given deformations. Although the results of the strain rates are more variable than the strain results, this is most likely due to numerical error introduced by differentiation.

Twist values demonstrated little change around the annulus over the cardiac cycle (Fig. 8). Only at areas adjacent to crystal 4 and crystal 10 did the twist values deviate from unity: in the mid-anterior leaflet region (crystal 4), twist values reached a minimum of near −8 degree/mm (negative values indicate counterclockwise rotation), while the min-posterior leaflet region (crystal 10) reached a maximum value of near 8 degree/mm (positive values indicate clockwise rotation). Bend values, as plotted in Fig. 9, showed a similar trend as twist, with minimal variation around the annulus and throughout the cardiac cycle, except near the mid-anterior leaflet region (reaching a minimum value of −7 degree/mm) and near the mid-posterior leaflet region (maximum value of 8 degree/mm).

Discussion

Because of the high temporal and spatial resolution (0.024 mm) of the piezoelectric sonocrystals used in this study, this work represents a more accurate attempt to investigate *in vivo* annular kinematics using a fully generalized description. Based on the quality of fit data, the technique described to capture the dynamic deformation of the annulus was successful and as such, provided a high-degree of accuracy in the computation of strain and strain rate information. Since crystal distances on the annulus were on average ~10 mm and the spatial resolution was 0.024 mm, it was reasonable to assume errors in strain and strain rate were negligible, as in our previous work.[42] Importantly, this technique provided a means to analyze *regional* deformation variations as well as determine other deformation measurement metrics such as bend and twist. Such information serves to elucidate the structure–function relationship of the MV while providing important regional boundary condition information for implementation into improved finite element models.

Strain and Strain Rate Relationships to Annular Structure

The MV leaflet (anterior) has previously been described as highly dynamic, showing mean peak areal strains up to 20% and mean peak strain rates up to 400%/s during a normal cardiac cycle.[38] Though previous studies have alluded to the dynamic nature of the annulus using radiopaque bi-plane videofluoroscopy perimeter measurements[46] and pulsed Doppler tissue imaging,[43] this work quantitatively reveals strain and strain rate information along the annulus. A major advantage of the present approach is the capability of analyzing strain and strain rate variations as both functions of time (throughout the cardiac cycle) and position, providing distinct visualization modalities (Figs. 4, 5). Both types of data presentation reveal interesting strain variations. It is evident that the commissure regions (crystals 1, 2 and 6, 7) are less dynamic, and collectively they strain minimally along the annulus (Figs. 3, 4, 5). Structurally, these areas consist of the left and right trigone edges where the fibrous annular

tissue thins into more muscular tissue.[25] The regions are less intimate with the aortic valve (compared to the anterior leaflet) yet still include fibrous tissue (as opposed to the posterior leaflet). Figure 5 shows strain versus time for specific crystals; compared to the other crystals, the commissure region crystals show little strain (4–5% maximum contraction) often with minimal error.

The anterior leaflet annular region (crystals 3, 4, and 5) and the posterior leaflet (crystals 8–12) annular region show increased strain variation both with time and position, though both leaflet regions show different trends. Around the anterior leaflet, contraction is observed during diastole, most notably near the posterior commissure side; systole shows little strain change (Fig. 5). It is surmised that the annulus anterior leaflet region, consisting of more fibrous tissue, could help dampen possible annular changes (and thus leaflet coaptation changes) during loading of the MV with subsequent opening of the aortic valve. Timek *et al.*[46] shows a similar trend; in this study, the perimeter change in the fibrous annulus (anterior leaflet region) showed little change through systole and a slight change during diastole (not statistically significant though). The posterior leaflet region shows increased contraction (upwards of 10%) during systole with similar values across the entire region, similar again to the Timek *et al.*[46] study. Intuitively, this is expected, as the muscular free-wall side of the posterior leaflet region is prone to increased contraction as ejection occurs and the mitral valve closes. Such action could serve to strengthen the coaptation between leaflets (reducing orifice area) to aid in preventing regurgitation. Specific crystal strain–time variations are observed (Fig. 5), further illustrating the large contractions seen during systole.

The annular strain rate variations (Fig. 6), further reveal the highly dynamic nature of the MV annulus. As expected from similar plots of strain results (Fig. 4), maximum strain rates are observed preceding maximum strain values for a given region. For example, as maximum strain is observed during systole for the posterior leaflet annular region, maximum strain rate is seen at the end of diastole. Consistent trends are observed for the anterior leaflet annular region and the commissure annular regions (Fig. 7). As in the strain vs. time plots for various crystal locations, the commissure region crystals shows minimal strain rate values over the measured cardiac cycle, while the annular regions surrounding the leaflets—especially the posterior leaflet region—shows maximum strain rate values of 120%/s (reached within the last quarter of the cycle). Further, the annulus region around the posterior leaflet displays a steeper decay of strain rate following the 120%/s spike, consistent with the structural differences discussed above.

The twist and bending data highlight some additional regional variations in the dynamic nature of the MV. As shown (Fig. 8), peak twist values are reached near both mid-leaflet regions (crystal 4 and crystal 10), but deviate little from unity along the rest of the annulus throughout the cardiac cycle. These peak values are reached at different times; the mid-anterior leaflet region shows deviation throughout most of diastole (Fig. 8), while the mid-posterior leaflet region shows the greatest departure from unity through most of systole. Similarly, the bending data mimics that of the twist data, with peak values reached near the mid-posterior leaflet region throughout most of systole (Fig. 9). It is important to note, however, that although it is possible to speculate as to the cause of these deviations from unity, such results may be an artifact from numerical error. Aside from these deviations, the rest of the annular region shows little change from unity throughout the cardiac cycle indicating that nearly all of the kinematic motion observed is through annular dilation/contraction. The limited change in annular height further supports that much of the kinematic motion is attributed to annular dilation/contraction.

Comparison to Previous Studies

This work provides a novel method for quantitatively determining 3D annular kinematics. A number of previous studies have attempted to, in part, characterize some degree of annular motion. Stoylen *et al.*,[43] Caiani *et al.*,[9] and George *et al.*[15] all utilized a form of Doppler tissue imaging to determine annular velocity, strain, and strain rate. These studies, however, were limited to a 2D analysis of annular deformation and relied on image tracking to calculate the kinematic descriptors. No true 3D information could be obtained from the experiments (though multiple 2D planes images were taken), and little regional kinematic information was available. Because of the nature of data measurement, twist or bending motion could not be calculated. Hayashi *et al.*[23] compared a variety of imaging techniques, including M-mode echocardiography, anatomic M-mode echocardiography, tissue Doppler displacement, and 2D strain imaging echocardiography, to assess annular motion. These techniques showed some variability, and results often depended on the imaging plane and transducer position. Ahmad *et al.*[2] and Timek *et al.*[46] both attempted to obtain 3D kinematic data using 3D echocardiography and bi-plane videofluoroscopy techniques; all three groups failed to obtain discrete regional 3D kinematic motion and deformation. Again, these groups were not capable of investigating twist or bending motion. Though basic kinematic information can be taken from these studies, an improved MV finite element model requiring detailed boundary condition information is not satiated by such results. The lack of regional information limits fundamental analyses of structure-function relationships of the annular tissue and hinders further annuloplasty ring developments.

Improved Modeling for Valve Therapies

A fundamental assumption in valvular therapies is that a repaired valve or valve replacement should mimic the functionality of the native MV as closely as possible. Thus, improvements in valvular treatments are dependent on the establishment of a complete understanding of the function and mechanical properties of the native normal MV. Finite element analysis has been extensively utilized for the analysis of native and prosthetic valve mechanics.[44] Although initially conducted with simplified material models, finite element modeling studies have shown that by changing valve design, such as using difference manufacturing techniques,[30] changing leaflets shapes,[20,30] and frame mounting methods,[7,8,27,30] the stress distribution pattern acting on the leaflets could be altered. Particular challenges are encountered in numerical[43] simulations of valvular function, including nonlinear anisotropic leaflet mechanical properties, leaflet contact, and experimental validation. Especially, experimental measurements of leaflet strain for validation are difficult to perform because of practical limitations in obtaining measurements very close to the leaflets and valve housing. Thus, previous finite element studies offered no experimental validation[4,21,26,31] or simple validations that only demonstrate comparisons with pulse duplicator images.[6,27] Only in a recent study[44] where the actual properties of individual leaflets and thorough experimental validation utilized together to produce actual simulations that were also carefully validated. Parametric studies utilizing the material parameter set from one leaflet for all three leaflets resulted in substantial variations in leaflet stress and strain distributions. This result suggests that utilization of actual leaflet material properties is essential for accurate finite element simulations, and underscores the need for rigorous experimentation and accurate constitutive models in simulating valve function. Paramount to the understanding and modeling of MV function is the availability of accurate boundary conditions of the annulus. With the current work, detailed information regarding annular motion and deformation is calculated from *in vivo* measurements. Further, this data is available along the entire annular surface from the shape element curve fitting technique, providing continuous strain and strain rate information. As a result, future modeling efforts will be able to incorporate this detailed 3D kinematical information of the annulus to help elucidate stress development in the MV leaflets.

Additionally, this information will assist in the development of a multi-scale model of the MV that incorporates mechano-transduction effects to help reveal valve repair capabilities and MVIC response. Annular boundary conditions may play an important role in leaflet stress and resultant MVIC action, as hinted at by Quick *et al.*[35] In this work, procollagen results (as a measurement of collagen synthesis) indicated that MV collagen synthesis was upregulated by factor of 1.8 in both the MR and abnormal ventricle wall motion (AVWM) ovine groups vs. controls. In addition, results showed greater upregulation in anterior leaflets compared with posterior leaflets in both infarct groups. These results indicate that MV collagen synthesis is upregulated in response to MR and AVWM and show a collagen synthesis difference between leaflets. The annular strain and strain rates, as discussed in the current work, vary based on the location along the annulus and could have an impact on the difference in leaflet collagen synthesis observed Quick *et al.*[35] In the very least, it exposes an exciting and interesting hypothesis to be tested.

Study Limitations

Though the experimental method provides exceptional *in vivo* results, the invasive surgical procedure limits the applicability to human studies. The use of ovine models may also present some differences compared to human models, i.e., difficulty in locating the true fibrous portion of the annulus in humans[3] and the possibility of increased myocardial motion in ovine models.[41] The use of twelve crystals provided enough experimental data to produce an accurate and faithful curve fit, though in three animals, crystals were lost. This complicated the Sobolev smoothing procedure; however, the quality of fit showed minimal changes with the reduction of single crystals. Use of more crystals in future studies could help prevent such problems and would ease the Sobolev smoothing process, though more crystals would not have a substantial impact on the quality of fit.

Summary

In this current work, a detailed method for accurately capturing complex 3D kinematics of the MV annulus is discussed. The described technique provides a means to faithfully reproduce annular motion and quantify strain and strain rate information along the entire annulus based on generalized highly accurate and validated shape element curve fitting. The results discussed reveal differences in strain and strain rate both spatially and temporally and highlight that the deformation of the annulus is complex and regionally variant. Interestingly, it was found that the annulus deforms mainly by axial strain, with mild height changes and low twisting/bending observed. This complexity further indicates that a better understanding of annular boundary conditions is critical for improved MV simulations.

Acknowledgments

This work was made possible by NIH Grant HL-073021NIH, an American Heart Association Pre-Doctoral Fellowship (CEE), the NIH/NIBIB T32 “Biomechanics in Regenerative Medicine” training Grant (NIBIB T32 EB003392-01).

Appendix

Appendix A—Quintic Hermite Shape Functions

The six shape functions N_α^i of the 1D quintic finite element used in this study are defined as follows[24]:

$$
\begin{aligned}
N_1^0 &= -\tfrac{1}{16}(\xi-1)^3\left(3\xi^2+9\xi+8\right)\\
N_1^1 &= -\tfrac{1}{16}(\xi-1)^3(3\xi+5)(\xi+1)\\
N_1^2 &= -\tfrac{1}{16}(\xi-1)^3(\xi+1)^2\\
N_2^0 &= \tfrac{1}{16}(\xi+1)^3\left(3\xi^2-9\xi+8\right)\\
N_2^1 &= -\tfrac{1}{16}(\xi+1)^3(3\xi-5)(\xi-1)\\
N_2^2 &= \tfrac{1}{16}(\xi+1)^3(\xi-1)^2
\end{aligned}
\tag{A.1}
$$

where the subscript indicates the node number, the superscript the order of the derivative with respect to the local coordinate ξ, and the coordinate values at nodes 1 and 2 are −1 and 1, respectively.

Appendix B—Generalized Least Squares Regression

With the data properly oriented, the parameter estimation for the interpolation is done using the general matrix formulation for linear least squares. The function describing the component being fit is defined by:

$$
f = a_0\cdot\psi_0^0 + a_1\cdot\psi_1^0 + a_2\cdot\psi_2^0 + a_3\cdot\psi_0^1 + a\cdot\psi_1^1 + a_5\cdot\psi_2^1 + e \tag{B.1}
$$

where e is error and $[a]$ is a vector containing the nodal fit parameters for the function f. Expressed in matrix form the relationship can be written concisely as:

$$
\{f\} = [\psi]\{A\} + \{e\}\,. \tag{B.2}
$$

In this case, f is the component of the data being fit ($r(\theta)$ or $z(\theta)$) and e is the error associated with the fit at a given point. The rows of matrix $[\psi]$ are the shape functions evaluated at there isoparametric coordinate corresponding to the data point observed. It can be shown that the minimization of the sum square of errors associated with the partial derivatives of f with respect to each of the parameters can be reduced to the following expression:

$$
[\psi]^{\mathrm{T}}[\psi]\{A\} = \left\{[\psi]^{\mathrm{T}}\{f\}\right\} \tag{B.3}
$$

So the parameters are computed by simply inverting $[\psi]^{\mathrm{T}}[\psi]$ and left multiplying both sides of the equation. After estimating the parameters for each element, the curve can be interpolated by evaluating the polynomials for each element at any point within the domain. In the case of smoothing via the Sobolev algorithm, the Sobolev penalty function is added to the matrix $[\psi]^{\mathrm{T}}[\psi]$. The nodal parameters for the smoothed fit are computed using:

$$
A = \left[[\psi]^{\mathrm{T}}[\psi] + S\right]^{-1}\cdot\left[[\psi]^{\mathrm{T}} f\right] \tag{B.4}
$$

The described general matrix formulation for linear least squares is then used in the same manner to determine the parameters for each element.

References

1. Accola KD, et al. Midterm outcomes using the physio ring in mitral valve reconstruction: experience in 492 patients. Ann Thorac Surg 2005;79(4):1276–1283. discussion 1276–1283. [PubMed: 15797062]
2. Ahmad RM, et al. Annular geometry and motion in human ischemic mitral regurgitation: novel assessment with three-dimensional echocardiography and computer reconstruction. Ann Thorac Surg 2004;78(6):2063–2068. discussion 2068. [PubMed: 15561036]
3. Anderson RH, et al. The myth of the aortic annulus: the anatomy of the subaortic outflow tract. Ann Thorac Surg 1991;52(3):640–646. [PubMed: 1898167]
4. Black MM, et al. A three-dimensional analysis of a bioprosthetic heart valve. J Biomech 1991;24:793–801. [PubMed: 1752863]
5. Braunberger E, et al. Very long-term results (more than 20 years) of valve repair with Carpentier's techniques in nonrheumatic mitral valve insufficiency. Circulation 2001;104(12 Suppl 1):I8–I11. [PubMed: 11568021]
6. Burriesci G, Howard IC, Patterson EA. Influence of anisotropy on the mechanical behaviour of bioprosthetic heart valves. J Med Eng Technol 1999;23(6):203–215. [PubMed: 10738683]
7. Cacciola G, Peters GW, Baaijens FP. A synthetic fiber-reinforced stentless heart valve. J Biomech 2000;33(6):653–658. [PubMed: 10807985]
8. Cacciola G, Peters GW, Schreurs PJ. A three-dimensional mechanical analysis of a stentless fibre-reinforced aortic valve prosthesis. J Biomech 2000;33(5):521–530. [PubMed: 10708772]
9. Caiani EG, et al. Evaluation of alterations on mitral annulus velocities, strain, and strain rates due to abrupt changes in preload elicited by parabolic flight. J Appl Physiol 2007;103(1):80–87. [PubMed: 17615285]
10. Carpentier A. Reconstructive valvuloplasty. A new technique of mitral valvuloplasty. Presse Med 1969;77(7):251–253. [PubMed: 5795420]
11. Fasol R, et al. Mitral valve repair with the Colvin-Galloway Future Band. Ann Thorac Surg 2004;77(6):1985–1988. discussion 1988. [PubMed: 15172250]
12. Filip DA, Radu A, Simionescu M. Interstitial cells of the heart valve possess characteristics similar to smooth muscle cells. Circ Res 1986;59(3):310–320. [PubMed: 3769149]
13. Flameng W, Herijgers P, Bogaerts K. Recurrence of mitral valve regurgitation after mitral valve repair in degenerative valve disease. Circulation 2003;107(12):1609–1613. [PubMed: 12668494]
14. Gammie JS, et al. Trends in mitral valve surgery in the United States: results from the Society of Thoracic Surgeons Adult Cardiac Surgery Database. Ann Thorac Surg 2009;87(5):1431–1437. discussion 1437–1439. [PubMed: 19379881]
15. George K, et al. Mitral annular myocardial velocity assessment of segmental left ventricular diastolic function after prolonged exercise in humans. J Physiol 2005;569(Pt 1):305–313. Epub 2005 Aug 18. [PubMed: 16109725]
16. Gillinov AM, et al. Durability of mitral valve repair for degenerative disease. J Thorac Cardiovasc Surg 1998;116(5):734–743. [PubMed: 9806380]
17. Gillinov AM, et al. Cosgrove-Edwards Annuloplasty System: midterm results. Ann Thorac Surg 2000;69(3):717–721. [PubMed: 10750749]
18. Goldsmith IR, Lip GY, Patel RL. A prospective study of changes in the quality of life of patients following mitral valve repair and replacement. Eur J Cardiothorac Surg 2001;20(5):949–955. [PubMed: 11675179]
19. Gorman JH 3rd, et al. Dynamic three-dimensional imaging of the mitral valve and left ventricle by rapid sonomicrometry array localization. J Thorac Cardiovasc Surg 1996;112(3):712–726. [PubMed: 8800160]
20. Gould PL, et al. Stress analysis of the human aortic valve. Comput Struct 1973;3:377.
21. Hamid MS, Sabbah HN, Stein PD. Influence of stent height upon stresses on the cusps of closed bioprosthetic valves. J Biomech 1986;19:759–769. [PubMed: 3793750]
22. Hashima AR, et al. Nonhomogeneous analysis of epicardial strain distributions during acute myocardial ischemia in the dog. J Biomech 1993;26:19–35. [PubMed: 8423166]

23. Hayashi SY, et al. Analysis of mitral annulus motion measurements derived from M-mode, anatomic M-mode, tissue Doppler displacement, and 2-dimensional strain imaging. J Am Soc Echocardiogr 2006;19(9):1092–1101. [PubMed: 16950463]
24. Hinton, E.; Owen, DRJ. An Introduction to Finite Element Computations. 1st. Swansea, UK: Pineridge Press Limited; 1979. p. 385
25. Ho SY. Anatomy of the mitral valve. Heart 2002;88(Suppl 4):iv5–iv10. [PubMed: 12369589]
26. Huang X, et al. A two dimensional finite element analysis of a bioprosthetic heart valve. J Biomech 1990;23:753–762. [PubMed: 2384487]
27. Krucinski S, et al. Numerical simulation of leaflet flexure in bioprosthetic valves mounted on rigid and expansile stents. J Biomech 1993;26:929–943. [PubMed: 8349718]
28. Kunzelman KS, Reimink MS, Cochran RP. Annular dilatation increases stress in the mitral valve and delays coaptation: a finite element computer model. Cardiovasc Surg 1997;5(4):427–434. [PubMed: 9350801]
29. Kunzelman KS, Reimink MS, Cochran RP. Variations in annuloplasty ring and sizer dimensions may alter outcome in mitral valve repair. J Card Surg 1997;12(5):322–329. [PubMed: 9635270]
30. Leat ME, Fisher J. Comparative study of the function of the Abiomed polyurethane heart valve for use in left ventricular assist devices. J Biomed Eng 1993;15(6):516–520. [PubMed: 8277758]
31. Li J, Luo XY, Kuang ZB. A nonlinear anisotropic model for porcine aortic heart valves. J Biomech 2001;34(10):1279–1289. [PubMed: 11522307]
32. Messier RH Jr, et al. Dual structural and functional phenotypes of the porcine aortic valve interstitial population: characteristics of the leaflet myofibroblast. J Surg Res 1994;57(1):1–21. [PubMed: 8041124]
33. Mulholland DL, Gotlieb AI. Cell biology of valvular interstitial cells. Can J Cardiol 1996;12(3): 231–236. [PubMed: 8624972]
34. Nowicki ER, et al. Mitral valve repair and replacement in northern New England. Am Heart J 2003;145(6):1058–1062. [PubMed: 12796763]
35. Quick DW, et al. Collagen synthesis is upregulated in mitral valves subjected to altered stress. ASAIO J 1997;43(3):181–186. [PubMed: 9152488]
36. Rabkin E, et al. Evolution of cell phenotype and extracellular matrix in tissue-engineered heart valves during in vitro maturation and in vivo remodeling. J Heart Valve Dis 2002;11(3):308–314. discussion 314. [PubMed: 12056720]
37. Rabkin-Aikawa E, et al. Dynamic and reversible changes of interstitial cell phenotype during remodeling of cardiac valves. J Heart Valve Dis 2004;13(5):841–847. [PubMed: 15473488]
38. Sacks MS, et al. In vivo dynamic deformation of the mitral valve anterior leaflet. Ann Thorac Surg 2006;82(4):1369–1377. [PubMed: 16996935]
39. Sacks MS, et al. In vivo biomechanical assessment of trigycidylamine crosslinked pericardium. Biomaterials 2007;28(35):5390–5398. [PubMed: 17822757]
40. Salgo IS, et al. Effect of annular shape on leaflet curvature in reducing mitral leaflet stress. Circulation 2002;106(6):711–717. [PubMed: 12163432]
41. Sands MP, et al. An anatomical comparison of human pig, calf, and sheep aortic valves. Ann Thorac Surg 1969;8(5):407–414. [PubMed: 5353458]
42. Smith DB, et al. Surface geometric analysis of anatomic structures using biquintic finite element interpolation. Ann Biomed Eng 2000;28(6):598–611. [PubMed: 10983706]
43. Stoylen A, et al. Strain rate imaging in normal and reduced diastolic function: comparison with pulsed Doppler tissue imaging of the mitral annulus. J Am Soc Echocardiogr 2001;14(4):264–274. [PubMed: 11287889]
44. Sun W, Abad A, Sacks MS. Simulated bioprosthetic heart valve deformation under quasi-static loading. J Biomech Eng 2005;127(6):905–914. [PubMed: 16438226]
45. Taylor PM, et al. The cardiac valve interstitial cell. Int J Biochem Cell Biol 2003;35(2):113–118. [PubMed: 12479860]
46. Timek TA, et al. Aorto-mitral annular dynamics. Ann Thorac Surg 2003;76(6):1944–1950. [PubMed: 14667619]

47. Yacoub M, et al. Surgical treatment of mitral regurgitation caused by floppy valves: repair versus replacement. Circulation 1981;64(2 Pt 2):II210–II216. [PubMed: 7249325]

48. Young AA, Hunter PJ, Smaill BH. Estimation of epicardial strain using the motions of coronary bifurcations in biplane cineangiography. IEEE Trans Biomed Eng 1992;39(5):526–531. [PubMed: 1526643]

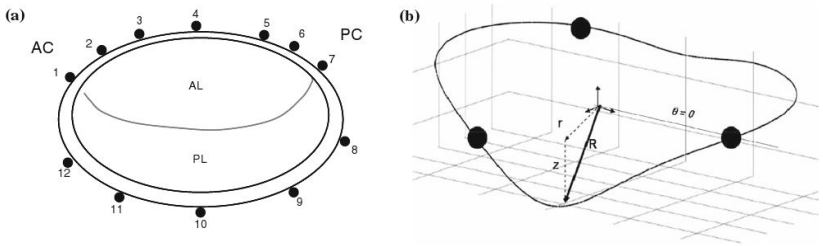

FIGURE 1.

(a) Sonocrystal placement around the annulus. Twelve crystals were used spaced on the annulus around both leaflets. (b) Coordinate system and element boundaries used in the quintic fit. A cylindrical coordinate system was used, and elements were of equal length.

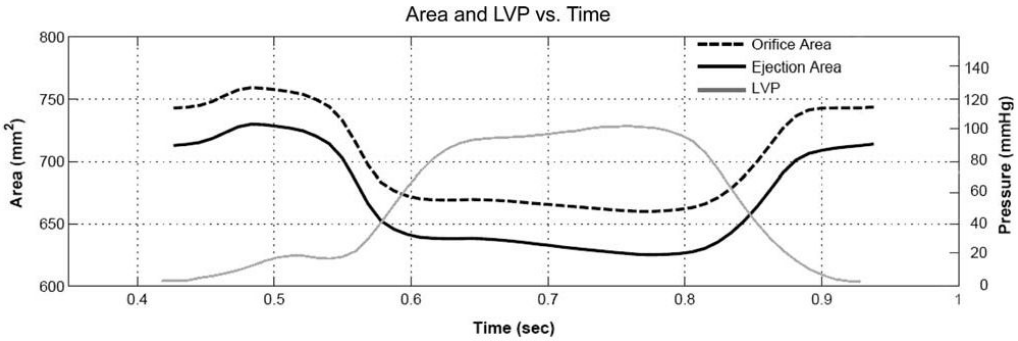

FIGURE 2.

Left ventricular pressure, orifice area, defined by the area of the cylindrical component position vectors, and ejection area, defined as the area of the orthogonal annular projection onto the *XY* plane, vs. time for a representative data set.

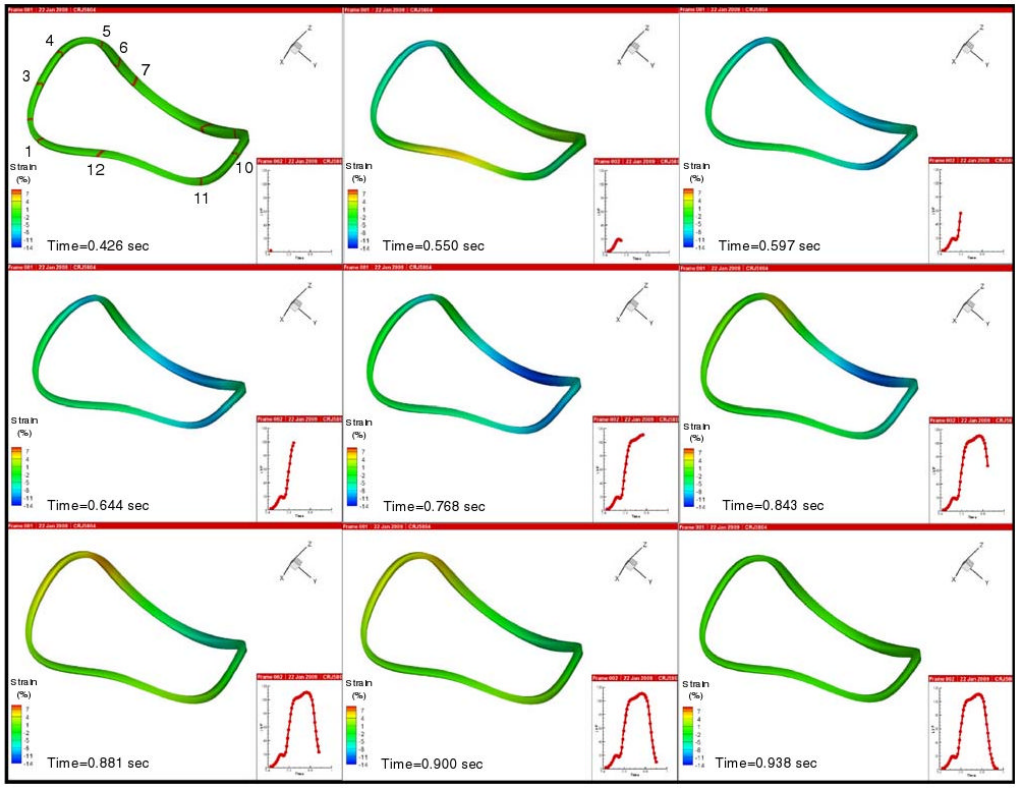

FIGURE 3.

Representative annular strain time snapshots throughout an entire cardiac cycle. The annulus was idealized as a 3D chord based on the 300 interpolated position and stretch data points. Numerals around annulus in top left pane indicate crystal number.

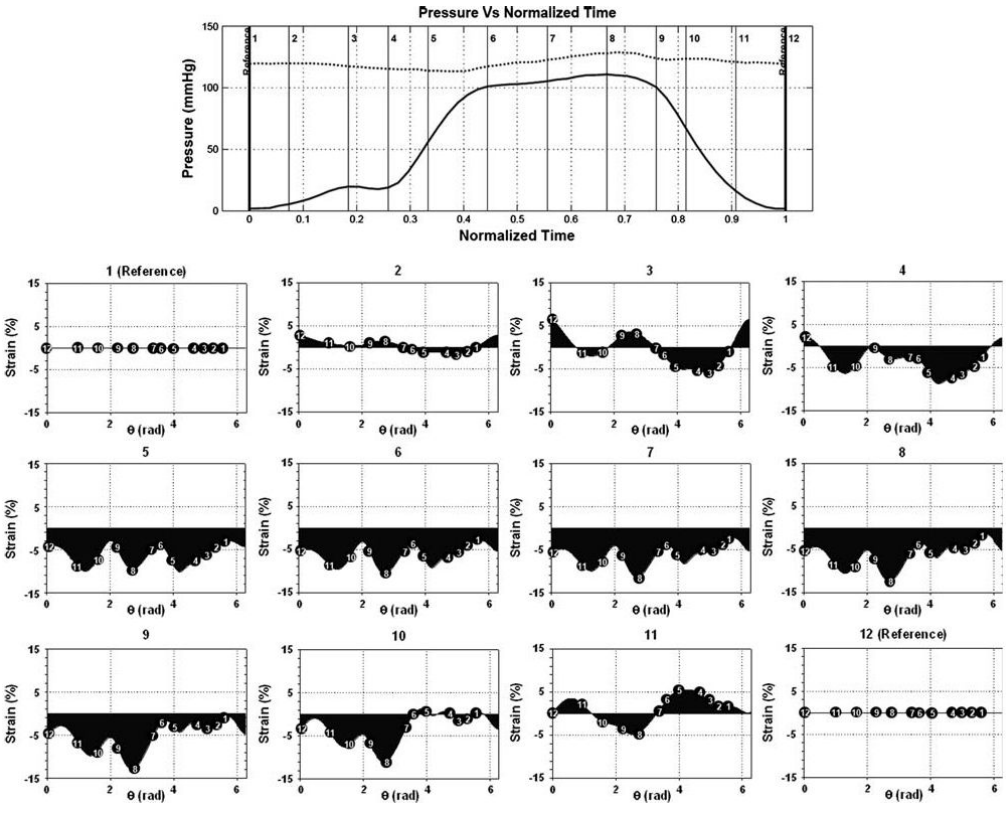

FIGURE 4.

Strain at various points in the cardiac cycle for a representative data set. Note both regional and temporal strain variations. All deformations are referenced to end diastole.

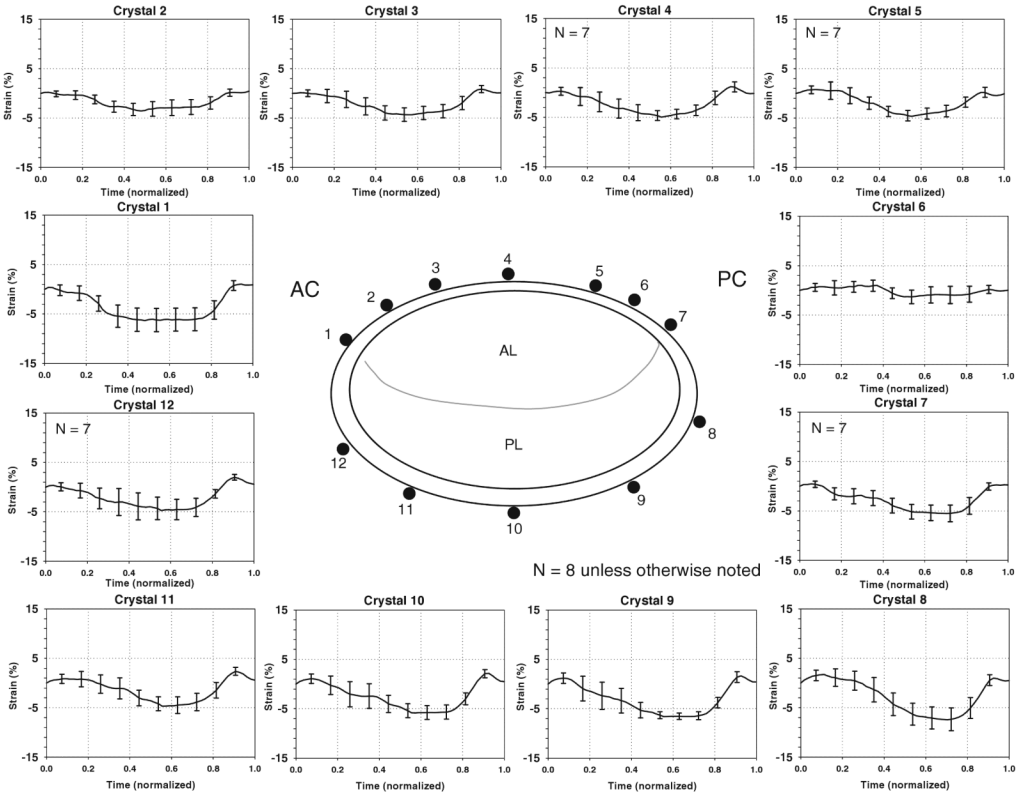

FIGURE 5.

Strain vs. time for specific sonocrystals around the annulus (*N* = 8 for each crystal unless otherwise noted). Values are plotted as mean ± SEM vs. normalized time. Commissure crystals show little strain through the cardiac cycle, while the posterior leaflet side (most notably the muscular free-wall side) shows the greatest strain values.

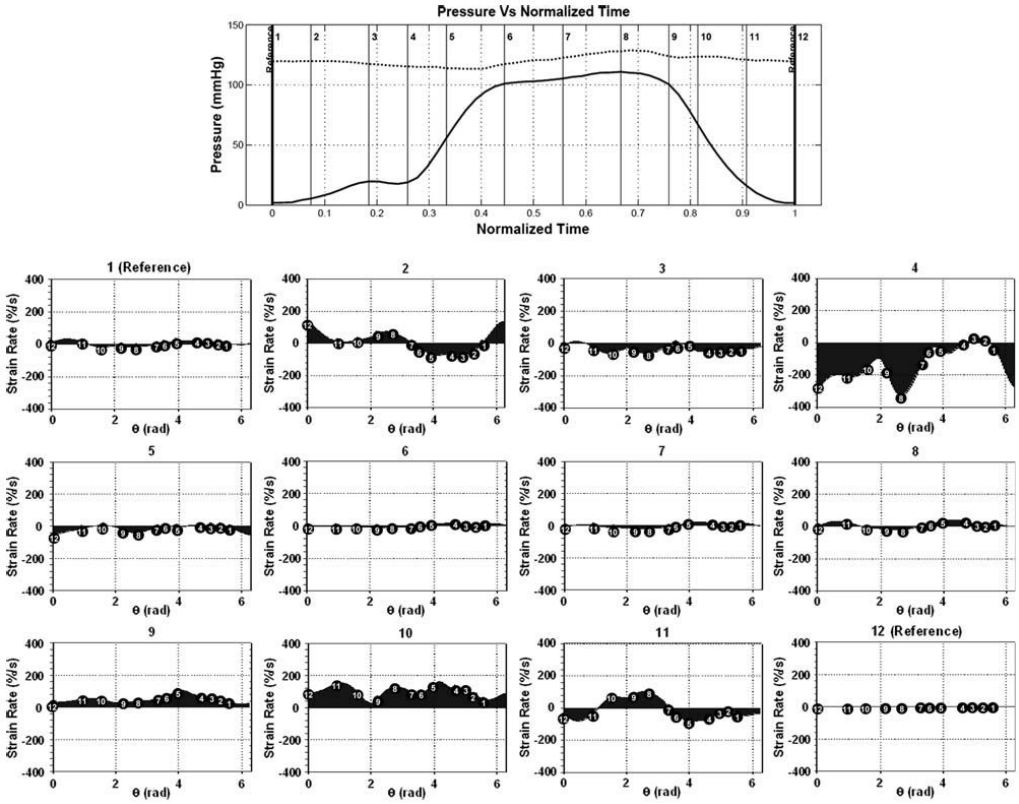

FIGURE 6.

Strain rate at various points in the cardiac cycle for a representative data set. As with strain, strain rate varies both regionally and temporally. All deformations are referenced to end diastole.

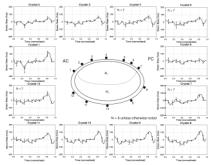

FIGURE 7.
Strain rate vs. time for specific sonocrystals around the annulus (N = 8 for each crystal unless otherwise noted). Values are plotted as mean ± SEM vs. normalized time. As with strain, strain rate shows greater values around the leaflet edges as compared to the commissure regions.

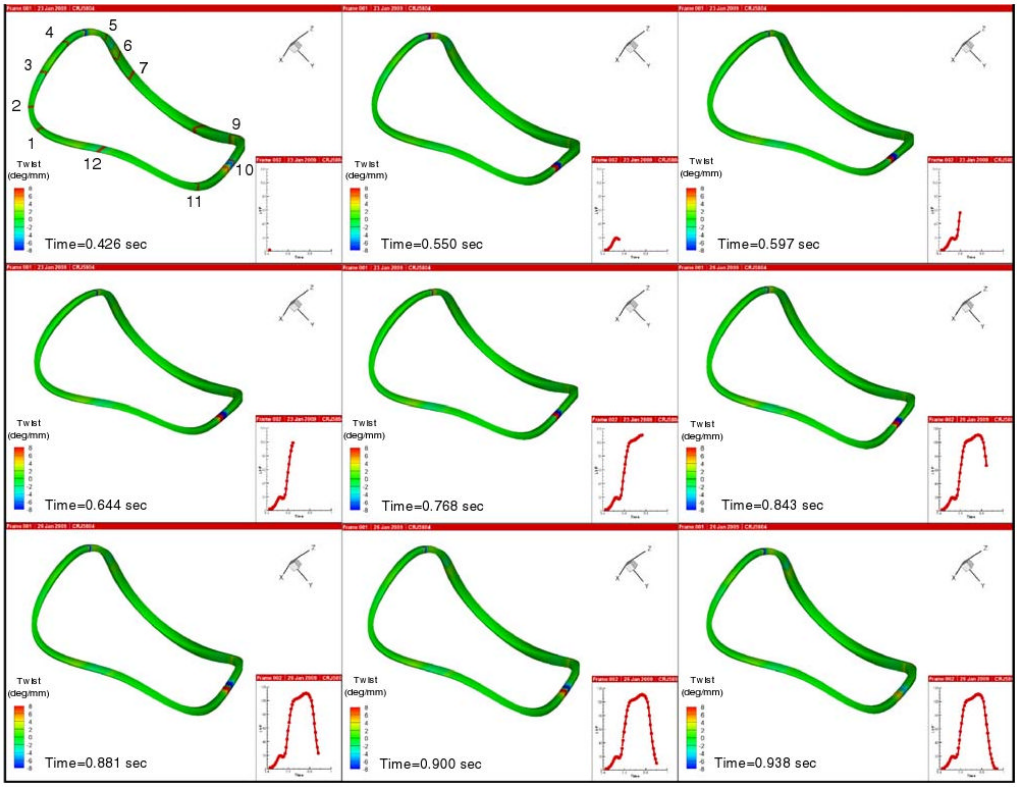

FIGURE 8.

Representative annular twist time snapshots throughout an entire cardiac cycle. Note that little change in twist occurs throughout time, implying that the annulus wastes little energy to excess motion. Numerals around annulus in top left pane indicate crystal number.

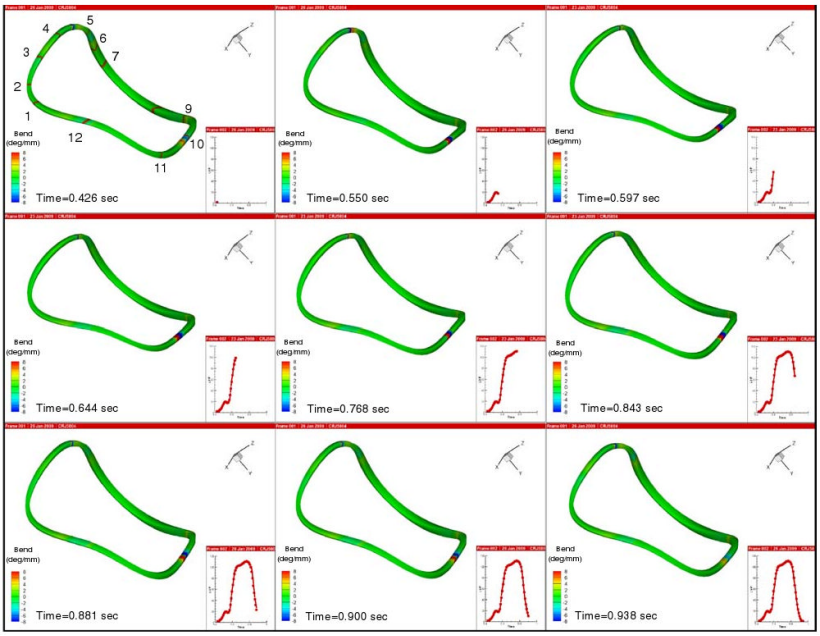

FIGURE 9.

Representative annular bend time snapshots throughout an entire cardiac cycle. Note that little change in bending occurs throughout time, as in the twist plot, indicating that little energy is wasted to excess annular motion. Numerals around annulus in top left pane indicate crystal number.